A case study in archaeomagnetism: how can we detect heat treatment in silcrete?

Eliza Poggi

Yale Department of Earth and Planetary Sciences

Readers: Dr. Ellery Frahm, Dr. David Evans

December 21, 2022

Abstract

Identification of heat treatment in raw materials used by early humans to make stone tools is critical to the study of ancient pyrotechnology. Silcrete, a chemically heterogeneous sedimentary rock produced by cementation of silica, is a major constituent of stone tools found in Middle Stone Age (~300 ka-20ka) sites, particularly in modern South Africa. The study of archaeomagnetism applies concepts of paleomagnetism, the study of Earth's magnetic field and the behavior of magnetic minerals, to human artifacts. Previous studies have employed archaeomagnetic techniques to examine heat treatment of silcrete tools. Ongoing studies at the Yale Archaeomagnetic Laboratory attempt to address 1) how heat treatment can be detected objectively in silcrete and 2) how heat treatment differentially affects silcrete sourced from various locations. Preliminary results indicate that due to variable mineralogical composition, in order to detect heat treatment in silcrete, samples must be compared in the context of other silcrete sourced locally. Color spectroscopy shows potential as a non-destructive method to identify heating of silcrete with magnetic mineral assemblages in an oxidative environment.

Chapter 1: Silcrete geologic background

1. A. Silcrete petrogenesis

Silcrete is a broad term used to refer to duricrust produced by cementation of unconsolidated sediments or by silica in crystalline or amorphous phases, often in outcrops bordering ephemeral bodies of water. A more specific term, *silcrete-calcrete intergrade duricrusts*, first introduced by

Nash & Shaw (1998), considers that silcrete and calcrete duricrusts often occur not as a homogenous material but as a mixture of SiO_2 and $CaCO_3$ precipitates, either where secondary calcite occurs within a siliceous matrix, secondary silica occurs within a calcareous matrix, or silica and calcite precipitate contemporaneously. Authigenic silica can precipitate in calcrete by filling voids or veins, replacing carbonate alo9ng the margins of voids, or replacing the calcite matrix itself (Nash & Shaw, 1998). Duricrusts containing calcite and silcrete that have precipitated contemporaneously are relatively uncommon but have been reported from the Sowa Pit, Botswana, and are thought to have formed as a result of cyanobacterial activity (Nash & Shaw, 1998).

Silcrete formation can occur by different mechanisms, each with implications for paleoenvironments of formation (Ullyott & Nash, 2016). Pedogenic silcrete describes silcrete formed by precipitation from solutions moving downward through soil; these outcrops are formed as silica and other cations are precipitated as a result of alternating wet and dry periods (e.g., Thiry & Milnes, 1991). Pedogenic silcrete is associated with the formation of paleosurfaces and forms over large areas over a timescale on the order of less than 10^6 years (Thiry & Milnes, 1991). In contrast, the formation of non-pedogenic silcrete is a more localized process on the timescale of thousands of years, related to the location of the water table, and does not have implications for the location of paleosurfaces (Thiry & Ribet, 1999).

Silcrete can refer to materials of various structure and fabric. Summerfield (1983a) classifies silcrete fabrics sourced from the Kalahari Basin into four major types: grain-supported, floating, matrix, and conglomeratic, describing silcrete in which skeletal grains are in contact with each

other, skeletal grains still maintain a significant proportion of the rock but exist within a finer-grained matrix, skeletal grains make up less than 5% of the rock by volume, or the rock contains relatively large pebbles, respectively. Silcrete *sensu stricto* refers to silcrete of over 85% silica (Summerfield, 1983a).

1. **B. Global distribution of silcrete**

Silcrete duricrusts can be found spanning the globe in fluvial depositional environments, but outcrops are often reported in the context of early human use of stone tools. This essay focuses primarily on silcrete sourced from the Kalahari Desert and Cape Coastal Region in southern Africa, but silcrete deposits have been documented in other regions, often using different terminology.

Silcrete was commonly used as a raw material for stone tools by Late Pleistocene Paleo-American hunter-gatherers in the southern tip of South America as early as ~13 and 12 ka (Nami, 2017). In South America, silcrete was commonly used as a raw material to make projectile points; however, complicating the South American record of silcrete is the simultaneous use of the terms "silcrete", "silicified limestone", "reddish limestone", and "carneolita" in the literature (Mazz, 2017). In the UK, historically the term "sarsen" has been used to describe allochthonous boulders composed of silica-cemented sands that occur particularly on the chalklands of southern England (Summerfield, 1979). The term "puddingstone" describes similarly silica-cemented boulders that exhibit a conglomeratic texture (i.e., rounded rather than angular clasts) (e.g. Summerfield, 1979). In Australia, silcrete outcrops

used for raw materials by early humans are of varying geochemical composition, resulting in varying color and mechanical properties including flaking properties, tensile strength, and elasticity (Webb & Domanski, 2008).

In South Africa, silcrete occurs bimodally in the Kalahari Basin and Cape Coastal zone. Kalahari Basin silcrete is formed through the silicification of a variety of host materials including calcretes and playa sediments (e.g. Summerfield, 1982). This is classified as "nonweathering silcrete" and is concentrated in areas where mineral-rich water is available to transport the sediment forming the matrix along playa margins, fossil river channels, and even at depth within the Kalahari Beds as demonstrated through borehole samples, possibly indicating transport of silica by groundwater (Summerfield, 1982). While silcrete within the Kalahari beds is associated with a range of continental deposits, silcrete in the Cape Coastal zone is often associated with weathering profiles of various lithologies including shales, phyllites, and tillites and can occur in layers up to 5 m thick (Summerfield, 1983b). Silcrete exhibits petrological features characteristic of both sedimentary rocks and soils, posing a unique challenge to classification; various classification schemes define classes of silcrete based on proportions of silica matrix to grains of other material, which are often metal oxides (Summerfield, 1983b). Certain petrographic features, including the presence of long-length chalcedony in vug-fills has directed several previous studies of Kalahari Basin silcrete (e.g., Collinson, 1978) to cite silcrete as an indicator of a semi-arid environment, although precipitation of titanite in silcrete sourced from Cape Coast, South Africa, has provided evidence that some silcrete experienced significant weathering, indicating a humid paleoclimate (Summerfield, 1983c).

1. C. Relevance of silcrete to the study of ancient pyrotechnology

The use of fire by hominids, claimed by some scholars to have started as early as 1.7 million years ago, has implications for the behavior, diet, technological development, and migratory patterns of early humans (James et al., 1989). However, the first evidence of heat treatment of lithics by early humans occurred in the Middle Stone Age, the transitory period in which archaic humans were gradually replaced by anatomical humans in Sub-Saharan Africa, with the earliest instance of heat treatment of lithics c. 164 ka from Pinnacle Point, South Africa (Brown et al., 2009). Identifying the processes by which lithics were transformed into stone tools by early humans is necessary to understand ancient technological evolution. Artifacts from contemporaneous archaeologic sites across South Africa show evidence of pressure flaking, a technique in which stone artifacts are sharpened using the narrow edge of a tool. Some materials, including obsidian, jasper, and some flints can be modified by pressure flaking without the use of heat treatment (Mourre et al., 2010). However, experimental replication of tools used by early hominids has shown that the majority of stone tools, including silcrete tools, require heat treatment, which allows for increased precision in forming narrowly tapered points, for shaping with pressure flaking (Mourre et al., 2010). Investigation into the ways heat treatment is recorded in silcrete is critical to inform future studies of the development of early human pyrotechnology.

1. D. Chemical changes to silcrete associated with heat treatment

The ability to modify silcrete through pressure flaking after heating results from a series of physical transformations that the material undergoes as heating progresses. Infrared-spectroscopy in conjunction with stepwise heating of silcrete by Schmidt et al. (2013) demonstrated that upon heating, silcrete will lose chemically bound water in the form of silanol and synthesis of molecular water (H_2O); at temperatures greater than 500°C, hydrolysis of silica hydrates contribute to fracturing of silcrete. Mackay et al. (2019) showed that, controlling for sample volume and heating rate, tensile failure as a result of heat treatment varies greatly between silcrete sourced from Australia and South Africa. In an effort to refine understanding of the differential effects of heat treatment on silcrete sourced from different outcrops within the same geographic region, Watson et al. (2021) sought to characterize how heat treatment affected silcrete differentially. The authors found that in addition to mineralogical variability, silcrete from different outcrops in the Kalahari Basin and Cape Coastal Zone also exhibited different starting concentrations of H_2O and SiOH, in addition to differing volumes of pore space (Watson et al., 2021).

1. E. Studies of silcrete geochemical variability

Locating the source of lithic raw materials is critical to understanding the development of lithic technology and associated trade routes. At individual silcrete sites, outcrops exhibit little chemical variability down-profile (Nash et al., 1994). However, within larger regions such as the

Kalahari Basin exists significant geochemical variability between silcrete outcrops. This variability is the basis for geochemical provenancing of silcrete tools, which can provide insight into human behavior.

Geochemical provenancing has been accomplished for MSA silcrete tools from both the Kalahari Desert and Cape Coastal Zone. Nash et al. (2013a) first describe a procedure for provenancing silcrete raw materials: inductively coupled plasma mass spectrometry (ICP-MS) and inductively coupled plasma atomic emission spectroscopy (ICP-AES) yield distinct geochemical profiles for silcrete sourced from the Boteti and Okavango rivers, Lake Ngami, and the Xaudum Valley, Botswana. A comparison of these profiles to those of silcrete tools found at the MSA site White Paintings Shelter suggested that inhabitants of that site, despite having access to a nearby silcrete outcrop at Tsolido Hills, Botswana, chose to source raw materials from the Okavango Delta over 220 km away (Nash et al., 2013a). In subsequent statistical analysis of silcrete from the Cape Coastal Zone, silcrete from 12 sites also showed statistically distinct geochemical profiles (Nash et al., 2013b).

Chapter 2: An introduction to archaeomagnetism and applications to silcrete

2. A. Magnetism background

2. A. I. Types of magnetic materials

Magnetization results from the spin states of electrons surrounding the atomic nuclei of a material. The magnetic moment of a material is a vector quantity with both magnitude and

direction. Six types of magnetism are recognized: diamagnetism, paramagnetism, ferromagnetism, antiferromagnetism, ferrimagnetism, and superparamagnetism. These forms of magnetism result from varying arrangements of electron spin states within different materials and can either be remanent (permanent) or induced (temporary). Diamagnetism, which can affect any material, refers to a weak form of magnetism resulting from the change of orbital motions upon exposure to an external magnetic field. Paramagnetic and superparamagnetic materials will also experience a temporary magnetic moment in the direction of an external magnetic field of a relatively smaller and larger magnitude, respectively. Ferromagnetism is a property of some electrically uncharged iron-bearing materials to experience permanent magnetic attraction to each other. Antiferromagnetism is similarly permanent but results from the arrangement of electrons in a manner that causes their electron spins to cancel; in minerals exhibiting canted antiferromagnetism, these spins are directed on an angle resulting in a net non-zero magnetic moment. Magnetic minerals include magnetite, hematite, goethite, and wüstite. Rocks consist of fine-grained ferromagnetic minerals within a matrix of paramagnetic and diamagnetic minerals. Rocks containing magnetite and hematite are preferred candidates for archaeomagnetic studies as they can acquire permanent magnetic signals as a result of their intrinsic characters, ferrimagnetism and canted antiferromagnetism, respectively.

2. A. II. Natural remanent magnetism

Magnetic minerals can acquire components of remanent magnetism through several means. Natural remanent magnetism (NRM) refers to the sum of remanent magnetism components in a rock, prior to any treatment in the laboratory. There are three common forms of NRM: thermal

remanent magnetism (TRM), chemical remanent magnetism (CRM), and detrital remanent magnetism (DRM). Of these, thermal remanent magnetism and its close relative, partial thermal remanent magnetism (pTRM), are the most useful to archaeomagnetic studies of heat-treated materials, as they are acquired during the process of heat-treatment. TRM is acquired when a mineral is heated past the Curie temperature, the point at which electron spins become aligned with the magnetic field, and subsequently cools. TRM is a vector sum of pTRM, consisting of separate components of magnetism that are acquired in distinct windows of "blocking temperatures." Through the acquisition of TRM components, ferromagnetic mineral-bearing rocks have the potential to record both a history of the paleodirection and paleointensity of Earth's magnetic field and a history of the silcrete's record of heating.

2. A. III. Magnetic susceptibility

Magnetic susceptibility is defined as the propensity of a given material to become magnetized by an external field and is equal to the ratio of magnetic intensity per unit volume to the strength of the applied field. Magnetic anisotropy results from a non-parallel alignment of the magnetic moment (a vector quantity representing magnetic strength and direction of an object) and the magnetization (the net magnetic dipole per unit volume). In anisotropic materials, magnetic susceptibility is expressed as a tensor, reflecting the 3-dimensional magnetization induced by a magnetic field, even if that field points only in a singular direction.

2. A. IV. Magnetic domains and anisotropy

Single-domain magnetism refers to the state of a ferromagnet in which magnetization is constant across the material. Materials with large grain size will exhibit multi-domain magnetism, in which the internal grain volume is composed of alternating "domains" of differently-directed magnetization that reduce the internal magnetic energy. The number of magnetic domains within a material decreases with decreasing grain size, until the grain size is small enough that it is no longer energetically favorable for multiple domains to coexist; at this size, grains are single domain. This *single-domain threshold grain size* is a function of saturation magnetization, or the maximum magnetization a material can experience when exposed to an external magnetic field, and grain shape. Hematite can be single-domain up to 15 μm, and magnetite can be single-domain up to 57 ± 5 nm (Butler, 1992, p. 32 ; Dunlop, 1972).

Magnetic anisotropy refers to the ways in which an object's magnetic properties are dependent on the dimensions of the object and its orientation relative to the external magnetic field. In most magnetically anisotropic materials, two directions, at an angle dependent on crystal symmetry, represent the preferred direction of magnetization (the "easy" axis) and the least preferred direction of magnetization (the "hard" axis). Magnetic anisotropy usually describes shape anisotropy, or anisotropy resulting from irregular dimensions of a mineral grain, but it can also result from the atomic structure of a crystal (magnetocrystalline anisotropy), tension (magnetoelastic anisotropy), or the interactions between antiferromagnetic and ferromagnetic materials (exchange anisotropy).

Magnetic anisotropy is a necessary property for a material to exhibit magnetic hysteresis. Magnetic hysteresis refers to the non-reversible behavior of a ferromagnetic object in the presence of an external field. "Hysteresis loops" are curves showing the relationship between external field strength H and magnetization M for a given material, and in archaeomagnetic studies are typically measured as closed circuits, in which the internal magnetic field is equal to the external magnetic field (Figure 1). Starting from a demagnetized magnet ($H = M = 0$), as the external field strength H increases, M will increase steadily until approaching an asymptote termed "magnetic saturation". If the external field then begins to decrease, M will follow a different curve, decreasing and intercepting the y-axis at the saturation remanence where H = 0. Then the curve will intersect the x-axis (M = 0) at the coercivity. Once the external field approaches a negative value of the same magnitude of the field at which magnetic saturation was reached, the curve will again approach an asymptote at the magnetic saturation, but in the opposite (negative) direction. The shapes of hysteresis loops vary depending on the magnetic properties of the materials. Hysteresis loop shape is dependent on grain size, which is related to grain volume which in turn affects magnetic saturation (Tauxe et al., 1996). Two endmembers of loop shapes are wasp-waisted and potbellied loops (Figure 1). Assuming single-domain behavior, the former cannot be generated by grains < 8 nm and the latter by grains > 30 nm (Tauxe et al., 1996).

2. B. Archaeomagnetic techniques

2. B. I. Archaeomagnetic dating

By the 1990s, archaeomagnetic dating as a method in archaeologic sciences had been well-established (e.g., Eighmy et al., 1990; Brown et al., 2021). Earth's molten iron core acts as an electromagnetic engine, resulting in a dynamic magnetic field that is generally aligned with the planetary spin axis. Magnetic minerals can preserve ferromagnetic remanence directions oriented relative to the contemporary position of Earth's magnetic poles. Archaeomagnetic dating involves thermal demagnetization of these rock samples, in which sequential heating in a zero-field environment removes magnetic components acquired by the specimen over geologic time. The remaining magnetism in the samples ideally record only the orientation of the rock relative to the pole during formation. Then, magnetic directions from multiple samples can be averaged and compared to time-calibrated secular variation curves and/or other samples to constrain their ages. Since archaeologic samples, especially fired clays containing magnetic minerals, have a more straightforward acquisition of remanent magnetism than sedimentary records and can be dated relatively precisely by association with an archeologic site, they are especially well suited for high-resolution studies of the intensity and direction of the geomagnetic field.

2. B. II. Archaeomagnetic provenancing

Archaeomagnetic signals preserved in obsidian tools can also be used to source the origin of the raw materials within a lava flow. Magnetic susceptibility and hysteresis parameters, as well as magnetic mineralogy, are distinct for sections within a lava flow (Frahm & Feinberg, 2013b).

Additionally, upon cooling, magnetic minerals in obsidian acquire a TRM component; archaeodirectionality studies can be used to source obsidian artifacts within a lava flow (Frahm & Feinberg, 2013b). If consistent with geochemical provenancing, archaeomagnetic provenancing can refine sourcing of raw materials used by early humans to make tools and provide insight into regional patterns of material procurement.

2. B. III. Archaeomagnetic analysis of silcrete

In recent years, burnt sediments have been shown to reliably record paleointensities and paleodirections (Calvo-Rathert et al., 2012 ; Carrancho et al., 2016). Experimental archaeologic studies have confirmed that silcrete, and colored, ferromagnetic mineral bearing sediment used for pigment becomes magnetized in fires simulating those of early humans, showing that archaeomagnetic analysis can determine whether an object has undergone heat treatment (Brown et al., 2009). Silcrete cooling after experiencing heating to temperatures above the Curie temperature for magnetite (575°C) and/or hematite (680°C), depending on composition, will acquire thermal remanent magnetism. Brain & Sillen (1988) showed that mineralogical changes to burnt bones from the Middle Stone Age (MSA) Site Swartkrans Cave, South Africa, were consistent with heating at 400-500°C. Later studies suggested that these bones, some of which exhibit butchery marks, were likely burned in an anthropogenic fire (Pickering et al., 2008). When cooling from these temperatures, silcrete containing magnetic minerals will acquire a partial thermal remanent magnetism (pTRM) component.

Chapter 3: Ongoing studies at the Yale Archaeomagnetic Laboratory

3. A. Introduction to silcrete experiments at the Yale Archaeomagnetic Lab, 2022

Silcrete was a critical material for the development of ancient pyrotechonology and is at the center of understanding human behavior in the Middle Stone Age. Previous studies have documented changes in color magnetic properties, flakeability, and tensile strength (e.g., Rowney & White, 1997; Brown et al., 2009; Schmidt et al., 2017) in silcrete associated with heat treatment. However, there is still a need for an objective, and ideally, non-destructive method to objectively identify heat treatment in silcrete tools. Relying on principles of archaeomagnetism, we intend to quantify the changes to silcrete associated with heat treatment, answering the following questions: 1) How can we identify objectively heat treatment in silcrete and how are they related to mineralogical changes upon heating? and 2) How are the effects of heat treatment differential among silcrete samples from different sources?

3. B. Materials and methods

3. B. I. Spring 2022 Preliminary Investigation

In Spring 2022, samples of silcrete sourced from four South African localities (nearest cities: Albertinia, Clanwilliam, George, Sedgefield, respectively) were selected for analysis due to their proximity to Middle Stone Age sites at Blombos Cave, Nelson Bay Cave, and Kangkara (Figure 2). Upon inspection these silcrete samples are visually consistent with stone tools recovered from

these sites (S. Watson, pers. comm.). As an outgroup, pedogenic silcrete from Hunter Valley, Australia, was also examined.

Specimens were prepared as non-oriented cubes (~1 cm in width) and labeled A (Albertinia), AF (Clanwilliam), G (George), S (Sedgefield), and HV (Hunter Valley). An L-Series Olympus Vanta portable X-ray fluorescence ("pXRF") device was used to characterize the elemental composition of each face of the silcrete cubes (Table 1). The silcrete cubes underwent thermal demagnetization in an oxidizing environment (temperature steps: 105°C, 150°C, 400°C, 500°C, 600°C, 700°C) in the two-layer Lodestar shielded room with using a commercial thermostat-controlled demagnetizer (ASC Scientific Model TD48) at the Yale Archaeomagnetism Laboratory, and magnetic direction and intensity were measured using an Agico JR6A Spinner Magnetometer. Before the first temperature step and after temperature steps 150°C, 400°C, 500°C, 600°C, and 700°C, each face of each cube underwent analysis with a Bartington MS2 Susceptibility Meter with MS2b Sensor (Table 2). Before and after the 150°C heating step, specimens were prepared from each sample by using a chisel to flake small (~2.2 mm) chips from blocks of silcrete; and hysteresis loops recording magnetic anisotropy were generated using a Princeton Measurements/Lakeshore Cryotronics 2900 Series Alternating Gradient Magnetometer (AGM).

3. B. II Ongoing experimentation beginning Fall 2022

In September 2022, analysis began of samples of silcrete sourced from the same outcrops as the silcrete investigated in Spring 2022. Four cubic specimens (~1 cm in width) were prepared from

each silcrete sample and labeled (Figure 5). The specimens were weighed, and pXRF and color spectroscopy measurements were completed with a StellarNet RPH12 Reflectance Probe on the same face for each cube (Table 3). A drying step in the ASC Scientific Model TD48 at 100 °C was completed; and the mass, pXRF, and color spectroscopy measurements were taken again. The cubes were then analyzed using a Thermo Phenom XL G2 Scanning Electron Microscope (SEM). Currently the samples are being prepared for thermal demagnetization in an oxidizing environment and analysis with the spinner magnetometer, similar to the procedure described in Spring 2022, although heating steps will be more frequent.

3. C. Preliminary results

3. C. I. Results from Spring 2022

Results from Spring 2022 led us to conclude that the majority of specimens from the chosen outcrops in South Africa (and Hunter Valley, Australia) were capable of preserving detectable magnetic signals indicative of heat treatment (Figures 3,4). The susceptibility meter showed that composition was relatively uniform across all faces of a given silcrete cube. Locality AF silcrete samples had significantly higher initial susceptibility.

AGM measurements consistently showed narrow hysteresis loops with a small coercivity, indicating that heating (e.g. by lightning strike) had not occurred before arrival at the lab, which would have affected future experiments. After heating to 105°C, the hysteresis loops generated

with measurements from the AGM were distinctly wider, indicating a stronger magnetic force required to reach the saturation point (Figure 3).

Three major trends emerged in mass susceptibility measurements that were taken after each temperature step during thermal demagnetization. At the 150°C step, samples from all outcrops experienced an increase in low-frequency susceptibility and a slight decrease in high-susceptibility frequency. At 700°C, all samples experienced a sharp increase in low-frequency magnetic susceptibility. At 500°C, the opposite pattern occurred, in which the silcrete specimens experienced a decrease in low-frequency susceptibility and a slight increase in high-frequency susceptibility (Figure 3).

Visual inspection of the specimens between temperature steps during the process of thermal demagnetization in an oxidizing environment to simulate early human fires showed that color of all of the specimens, but especially the initially redder AF specimens, became darker and more red. pXRF analysis showed that the AF specimens contained significantly more Ti and Fe than counterparts from other outcrops (Figure 3). AF specimens consistently had higher magnetic intensities compared to the other silcrete samples, and almost all samples displayed multi-component magnetism (Figure 4).

3. C. II. Results from Fall 2022

All measurements repeated before and after the drying step (heating to 100 degrees) stayed essentially constant; mass decreased by less than a milligram for each cube (Table 3). Color

spectroscopy measurements in Fall 2022 were consistent with first-order visual observations; the HV and AF specimens, which were redder than silcrete from other locations, have strong magnetic characteristics compared to other specimens. pXRF results were virtually the same from Spring 2022. SEM analysis provided insight into the mineralogical heterogeneity between the samples (Figure 6). Locality HV specimens were mostly silica matrix with small, isolated grains of iron oxides, aluminum oxides, and titanomagnetite. Locality G specimens were similarly composed with the addition of small mineral grains containing rare earth elements, including zircon and monazite. Locality A samples also contained zircon in addition to silica matrix, and iron oxides and small amounts of platinum were detected on the surface of the cube as well. Locality DM, the grayest of the specimens, contained the fewest number of grains of iron oxides, with occasional alkali cations within a silica matrix. However, locality AF (silcrete sourced from near Clanwilliam) was a clear outlier in terms of micro texture. These specimens contained a noticeably different silcrete fabric, with grains of silica in contact within a matrix composed of fine-grained iron oxides. The higher concentration of magnetic minerals in AF samples signaled a potential to record strong magnetic signals.

3. D. Discussion

The preliminary analysis of silcrete from the Spring 2022 samples indicated that the specimens studied in Fall 2022 should have the potential to faithfully record a history of heat treatment. To confirm that the samples had not been heated, hysteresis loops were also generated with measurements form the AGM after heating to 105 °C, which were distinctly wider, indicating a stronger magnetic force was required to reach the saturation point (Figure 4).

The increase in low-frequency magnetic susceptibility and decrease in high-frequency magnetic susceptibility at 150°C followed by the sharp increase in low-frequency magnetic susceptibility at 700°C indicated that when heated in an oxidative environment, the specimens experienced a transition from "hard magnet" mineralogy (i.e., a magnet composed mostly of single-domain grains) to "soft magnet" mineralogy (i.e., a magnet composed mostly of multi-domain grains, which are more conducive to flipping in the presence of a high-frequency field). The decrease in low-frequency susceptibility and a slight increase in high-frequency susceptibility at 500°C suggested a brief shift from softer to harder magnets. Notably the 700°C heating step was the first to occur after the Curie temperature of hematite (680°C) while the 500°C step corresponded roughly to the temperature at which magnetic mineral wüstite is formed at 450°C (Lin et al., 2017); it is possible that the shift in magnetic minerology was related to the formation of new iron-oxide minerals due to oxidation and heating in the oven. 500°C is also the temperature at which Schmidt et al., 2012 recorded internal fracturing to begin, allowing water previously contained in pores to evaporate, which also could affect hysteresis loops. Future thermal demagnetization experiments with more frequent temperature steps could refine the temperatures at which the silcrete experienced significant changes in magnetic properties, which could provide context into mineralogical changes occurring at those points.

pXRF analysis demonstrated significant chemical heterogeneity among the silcrete samples which was confirmed by EDS spectra. Notably, the silcrete fabric varies within these silcrete specimens; using guidelines from Summerfield, 1983a almost all of the specimens would be characterized as silica matrix-dominated ("M") with the exception of the AF samples, which

would be considered grain-supported ("GS"). The other silcrete samples both show at the

macroscopic level (by color) and microscopic level (by paucity of iron oxide grains) a lesser

concentration of magnetic minerals than the brick-red AF specimens. pXRF analysis in Fall 2022

demonstrated a significant percentage of iron and magnetite on the surface of the silcrete cubes

for all samples, but especially for AF, which was consistent with results from Spring 2022.

Previous experimental heating of silcrete specimens has demonstrated that source is the most

important determinant in differences to timescale of fracturing in heat-treated silcretes (Mackay

et al., 2018; Watson et al., 2021). As stepwise heating progresses, it is likely that the AF

specimens, which have the highest concentration of iron oxides, would record magnetization of a

higher intensity, as was observed in Spring 2022.

From the changes in magnetic anisotropy measurements from the AGM in Spring 2022, it

follows that the color changes observed upon heating the silcrete samples correspond to changes

in the magnetic minerology that accompany heating in an oxidative environment. Future

spectroscopy measurements will seek to characterize objectively color changes to the silcrete as

heating progresses.

3. E. Conclusions from 2022 experiments

At this stage, high-resolution stepwise heating has not been completed, which would show in

detail how mineralogical changes accompany given ranges of blocking temperatures, at which

different components of pTRM would be acquired. However, stepwise heating, in conjunction

with color spectroscopy measurements and AGM analysis, can shed light on the ways conditions

typical of MSA heat treatment of lithics cause changes in magnetic mineralogy and visual appearances of silcrete from various locations in South Africa. Silcrete composition varies from different outcrops, and/or from different regions within South Africa. Color spectroscopy remains a promising non-destructive method of detecting heat treatment in silcrete. However, while in the archaeological literature silcrete is used as a broad term to describe a class of raw materials used to make stone tools, in order to assess whether a given silcrete sample has undergone heat treatment it will be necessary to compare the sample to silcrete sourced from the same locality.

Human preference of one silcrete outcrop over another (e.g. as described in Nash 2013a) could be due to any number of factors; however, it is probable that amenability to being fashioned into sturdy tools provided significant value to a given outcrop. Still ambiguous is how different modes of silcrete formation contribute to forming raw lithics of with varying characteristics (i.e. fracture rate, flakability, tensile strength) that would affect the process of heat treatment to make stone tools. To investigate the relationship between the depositional mode of silcrete and associated chemical and microtextural characteristics in addition to differential responses to heat treatment, the field relationships of the outcrops must be examined. In addition to color spectroscopy, FTIR could be examined as another non-destructive method to identify heat treatment in silcrete, especially in museum settings. Following the work of Schmidt et al., 2017, using FTIR the presence/absence of silanol and molecular water could be determined in the silcrete samples. After heat treatment it would be expected that molecular water and not silanol would be present in the silcrete; measurements before heating could show how initial concentration of silanol and molecular water varies among the silcrete samples. This variation

could account for preferential use of one silcrete source over another as increased hardness in heat-treated silcrete has been attributed to the formation of Si-O-Si bonds related to the synthesis of water (Schmidt et al., 2012). Future study could also compare the experimentally heat treated silcrete samples with stone tools found from Nelson Bay Cave, Blombos Cave, and Kangkara, to determine how well our laboratory conditions emulated early human fires.

Figures
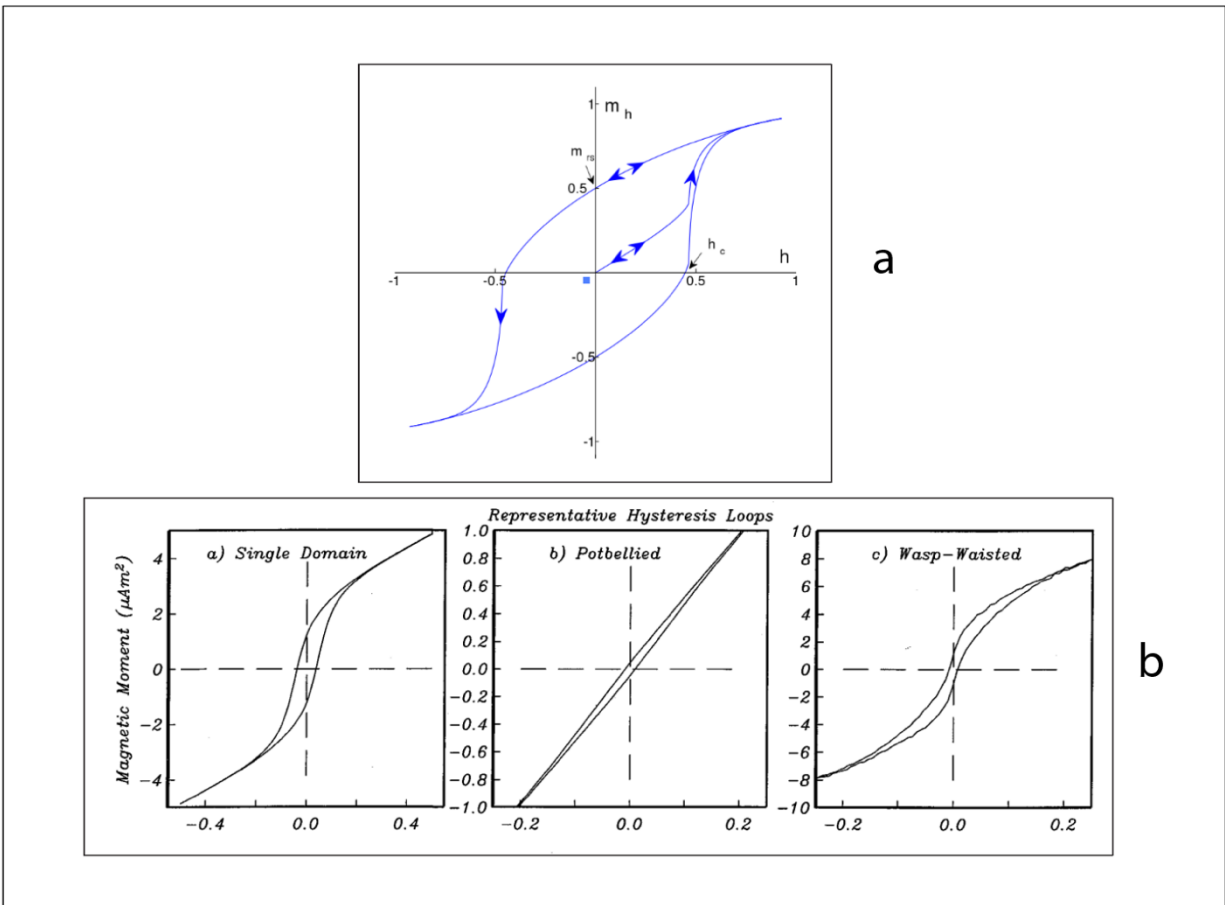
Figure 1. a: an example hysteresis loop showing the relationship between magnetization and strength of the external magnetic field. **b**: a figure adapted from Tauxe et al. (1996) showing differences in the shapes of hysteresis loops; wasp-waisted distortions cannot be generated by grains < 8 nm, and potbellied distortions cannot be produced by grains > 30 nm.

Figure 2. Field locations of silcrete samples and nearby MSA sites. Note that AF is sourced from the Kalahari Basin, rather than the Cape Coastal Zone. HV, examined as an outgroup, is from Hunter Valley, Australia.
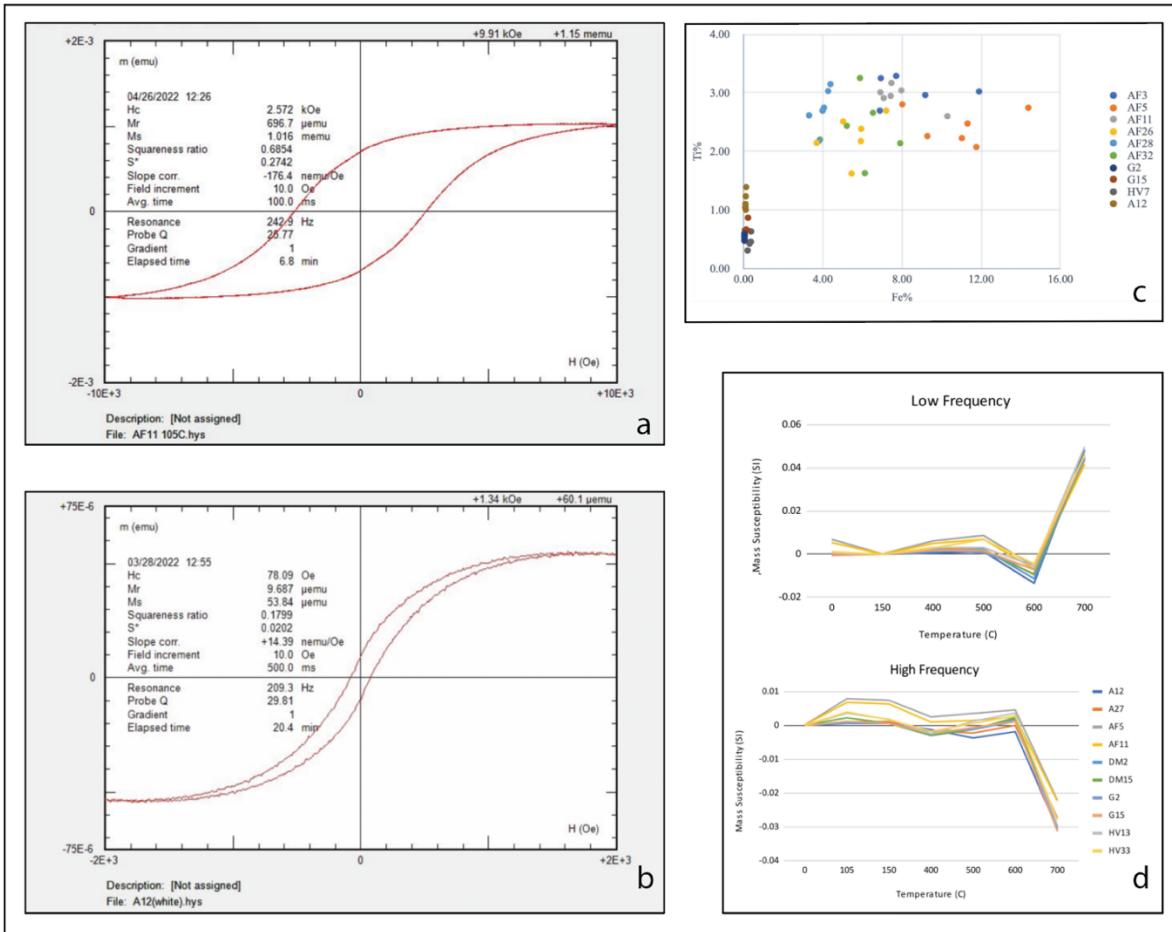
Figure 3. Hysteresis, chemical composition, and magnetic susceptibility from Spring 2022 preliminary investigation into silcrete sourced from Albertinia, South Africa, Clanwilliam, South Africa, George, South Africa, Sedgefield, South Africa, and Hunter Valley, Australia. **a**: a hysteresis loop from specimen AF11, after heating to 150 degrees C. Notice the wider shape compared to **b**: a hysteresis loop of A12 before heating that has a low coercivity and indicates **c**: pXRF analysis of samples. Note high Ti and Fe content for AF specimens. **d**: Mass susceptibility of silcrete samples. All follow the same general trends, showing changes especially at temperatures of 150°C, 500°C, and 700°C.
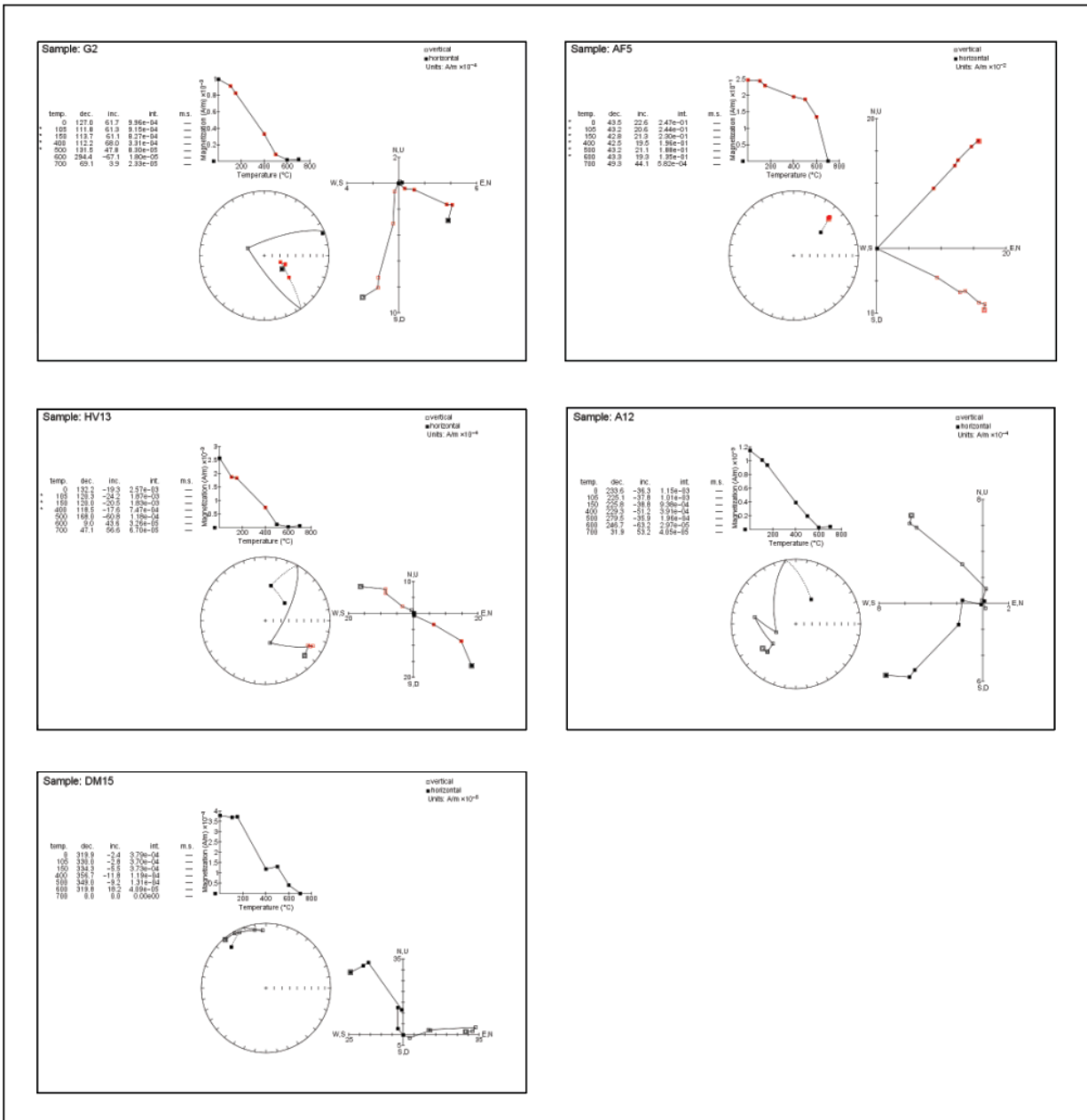
Figure 4. Results of low-resolution thermal demagnetization experiments, Spring 2022. Samples exhibit multi-component magnetism and appear to be fully demagnetized at the 700°C temperature step, coinciding with the Curie Temperature of hematite (680°C). More frequent temperature steps will be needed to characterize more precisely the different magnetic components acquired by the silcrete samples. Note the significantly higher initial magnetization of AF (Clanwilliam) silcrete compared to the other samples, on the order of 10^{-1} A/m compared to as low as 10^{-4}).
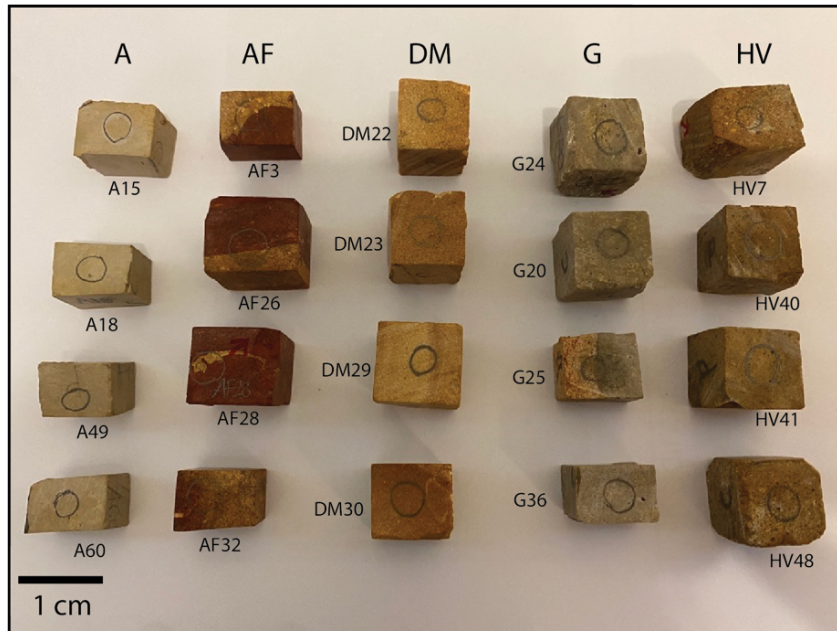
Figure 5. Silcrete sourced from Albertinia, South Africa (A), Clanwilliam, South Africa (AF), Sedgefield, South Africa (DM), George, South Africa (G), and Hunter Valley, Australia (HV). The circles designate the area in which color spectroscopy measurements were taken.
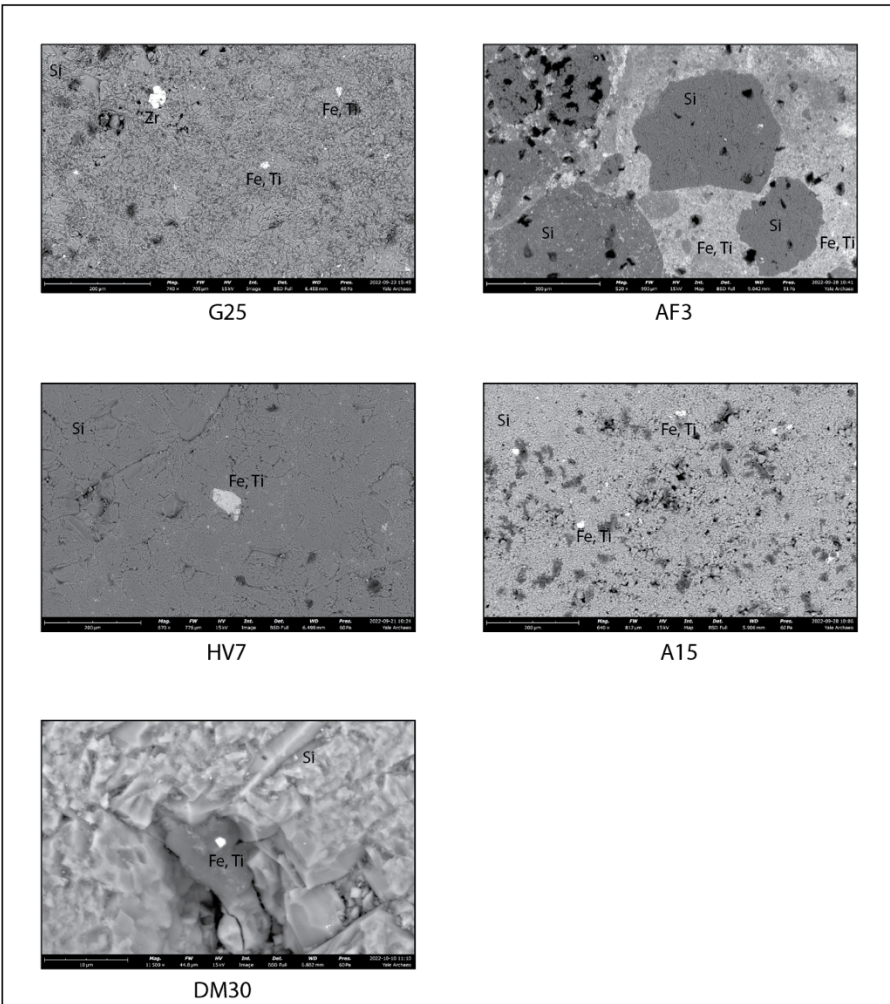
Figure 5. SEM images of silcrete studied Fall 2022. In samples G, A, DM, and HV, small grains of iron oxides, often containing small amounts of titanium, are supported within a silica matrix. Specimens sourced near George, South Africa (G) contain a significant number of anhedral zircon crystals. Clanwilliam silcrete (AF) consists of silica clasts within a matrix of fine-grained titanium and iron oxides.

Tables

Sample ID	LE Concentration	LE Error1s	Fe Concentration	Fe Error1s	Ti Concentration	Ti Error1s	Cr Concentration	Cr Error1s	Mn Concentration	Mn Error1s	Cu Concentration	Cu Error1s	As Concentration	As Error1s	Y Concentration
AF3a	56.1346	0.1541	6.8775	0.0277	2.6979	0.0248	0	0.0085	0	0.0937	0.004	0.0004	0.0024	0.0003	0.0019
AF3c	55.4841	0.1634	9.1677	0.0367	2.9631	0.0255	0	0.0086	0	0.0988	0.0037	0.0004	0.0023	0.0003	0.0018
AF3d	55.6769	0.1626	7.6983	0.0316	3.2895	0.0277	0.0067	0.002	0.0084	0.0016	0.0057	0.0005	0.003	0.0003	0.0026
AF3e	54.7449	0.1741	11.8877	0.0484	3.0242	0.0256	0.0097	0.002	0.0109	0.0018	0.0044	0.0005	0.0067	0.0004	0.0021
AF3f	56.3843	0.1566	6.9256	0.0283	3.2516	0.0272	0	0.0083	0.0262	0.0018	0.0051	0.0004	0.0026	0.0003	0.0028
AF5a	54.9808	0.17	11.0211	0.0444	2.2285	0.0221	0.0086	0.0019	0.0053	0.0016	0.0041	0.0005	0.0044	0.0003	0.0016
AF5b	56.1318	0.1589	8.0105	0.0322	2.8057	0.025	0.0069	0.0019	0.0051	0.0015	0.0039	0.0004	0.0028	0.0003	0.0021
AF5c	54.9429	0.1704	11.3053	0.0455	2.4774	0.0231	0.0079	0.0019	0.0056	0.0016	0.0049	0.0005	0.0053	0.0003	0.0018
AF5d	51.83	0.1845	14.3784	0.058	2.7471	0.0244	0.0125	0.0021	0.0148	0.0019	0.006	0.0006	0.0063	0.0004	0.0021
AF5e	55.7585	0.1627	9.2776	0.0371	2.2636	0.0223	0	0.0086	0.0066	0.0015	0.0049	0.0004	0.0045	0.0003	0.0017
AF5f	52.7867	0.1739	11.7485	0.0464	2.0769	0.0215	0.006	0.0019	0.0093	0.0017	0.0045	0.0005	0.0061	0.0004	0.0012
AF11a	56.267	0.1591	7.4622	0.0305	3.1691	0.0269	0.0062	0.0019	0.0129	0.0016	0.0046	0.0004	0.0022	0.0003	0.0023
AF11b	54.5462	0.161	7.9635	0.0317	3.0415	0.0262	0.0071	0.0019	0.0108	0.0016	0.0085	0.0005	0.0025	0.0003	0.0023
AF11c	56.1257	0.1576	7.4237	0.03	2.9474	0.0257	0.007	0.0019	0.0082	0.0015	0.0042	0.0004	0.0028	0.0003	0.0022
AF11d	56.522	0.1557	7.0688	0.0287	2.9123	0.0256	0.0078	0.0019	0.005	0.0015	0.0059	0.0004	0.0023	0.0003	0.0059
AF11e	56.488	0.1553	6.9046	0.028	3.0107	0.026	0.0081	0.0019	0.0055	0.0015	0.0039	0.0004	0.0031	0.0003	0.0021
AF11f	59.1413	0.1639	10.2909	0.0433	2.6028	0.0235	0.0079	0.0019	0.0055	0.0016	0.0086	0.0005	0.0054	0.0003	0.0016
AF26a	56.4928	0.156	7.1969	0.0291	2.6977	0.0246	0.0083	0.0019	0.0211	0.0017	0.0035	0.0004	0.0027	0.0003	0.003
AF26b	57.2156	0.141	3.6883	0.016	2.1484	0.0225	0.0068	0.0017	0	0.0915	0.0021	0.0003	0.0011	0.0002	0.0017
AF26c	57.0014	0.1484	5.9156	0.024	2.1783	0.0224	0.0065	0.0018	0.0058	0.0014	0.0023	0.0003	0.0022	0.0003	0.0017
AF26d	57.0635	0.1507	5.9322	0.0243	2.3866	0.0234	0.0054	0.0018	0.0062	0.0014	0.0024	0.0004	0.0023	0.0003	0.002
AF26e	57.4559	0.1448	5.0238	0.0208	2.5128	0.024	0.0106	0.0018	0.0045	0.0013	0.0023	0.0003	0.0013	0.0002	0.002
AF26f	58.8916	0.1443	5.4496	0.0224	1.6243	0.0193	0	0.0078	0.0155	0.0015	0.0021	0.0003	0.0012	0.0002	0.0012
AF28a	57.2212	0.1439	4.3827	0.0186	3.1501	0.027	0	0.008	0	0.0887	0.0036	0.0004	0	0.001	0.0023
AF28b	58.1373	0.1401	4.0559	0.0174	2.7482	0.025	0	0.0076	0	0.0889	0.0026	0.0003	0	0.001	0.002
AF28c	57.7085	0.1409	3.9879	0.0172	2.697	0.025	0.0084	0.0018	0.0042	0.0013	0.0024	0.0003	0.0009	0.0002	0.0029
AF28d	57.4	0.139	3.2986	0.0148	2.6174	0.0248	0.0082	0.0018	0	0.088	0.0023	0.0003	0	0.001	0.0022
AF28e	57.4612	0.1398	3.8014	0.0164	2.1809	0.0226	0	0.0074	0	0.0889	0.0026	0.0003	0.0008	0.0002	0.0017
AF28f	57.562	0.141	4.2607	0.018	3.0313	0.0261	0	0.0076	0.0054	0.0013	0.0029	0.0003	0	0.0009	0.0018
AF32a	57.8322	0.1417	3.8515	0.0167	2.205	0.0228	0	0.0075	0.0042	0.0013	0.0041	0.0004	0.0008	0.0002	0.0018
AF32b	58.1476	0.1508	5.8742	0.0245	3.2542	0.0272	0.0088	0.0019	0.0074	0.0015	0.0034	0.0004	0	0.001	0.0022
AF32c	57.2539	0.153	6.5295	0.0267	2.6604	0.0245	0.006	0.0018	0.0273	0.0018	0.009	0.0005	0.0013	0.0003	0.0035
AF32d	57.774	0.155	7.9068	0.0319	2.1416	0.0216	0	0.008	0.0264	0.0018	0.0037	0.0004	0.0018	0.0003	0.0019
AF32e	58.0845	0.1459	6.116	0.0245	1.6299	0.0191	0	0.008	0.0049	0.0013	0.0034	0.0004	0.0013	0.0002	0.0012
AF32f	58.5705	0.1462	5.2066	0.0218	2.4375	0.0235	0	0.0078	0.015	0.0015	0.0038	0.0004	0.0012	0.0002	0.0018
G2a	59.922	0.1191	0.0457	0.0014	0.5195	0.0125	0	0.0053	0.0031	0.001	0.0022	0.0003	0	0.0006	0.0011
G2b	59.9693	0.12	0.0352	0.0012	0.4776	0.0122	0	0.0057	0	0.0885	0.004	0.0003	0	0.0006	0.0012
G2c	59.1865	0.1196	0.0334	0.0012	0.4901	0.0123	0	0.0055	0	0.0867	0.0021	0.0003	0	0.0006	0.0014
G2d	57.9011	0.1162	0.029	0.0011	0.552	0.0124	0	0.0053	0	0.0805	0.002	0.0003	0	0.0006	0.0012
G2e	59.5285	0.1193	0.0344	0.0012	0.6016	0.0132	0	0.0054	0	0.0872	0.003	0.0003	0	0.0006	0.0013
G2f	59.6549	0.1189	0.0425	0.0013	0.5138	0.0124	0	0.0055	0	0.0892	0.0028	0.0003	0	0.0006	0.001
G15a	62.2411	0.1204	0.2162	0.0028	0.87	0.0152	0	0.0057	0	0.1064	0.0057	0.0003	0	0.0006	0.0012
G15b	60.4101	0.1202	0.0674	0.0016	0.6598	0.0137	0	0.0055	0	0.0927	0.005	0.0003	0	0.0006	0.0013
G15c	60.6968	0.12	0.0399	0.0013	0.5536	0.013	0	0.0056	0	0.0911	0.0018	0.0003	0	0.0006	0.0013
G15d	61.9478	0.1214	0.184	0.0026	0.6564	0.0137	0	0.0056	0.0032	0.001	0.0062	0.0003	0	0.0006	0.0014
G15e	60.2401	0.1223	0.1263	0.0022	0.6714	0.0139	0	0.0054	0	0.0951	0.0051	0.0003	0	0.0006	0.0014
G15f	60.4546	0.1199	0.0566	0.0015	0.5718	0.0131	0	0.0057	0	0.092	0.0023	0.0003	0	0.0006	0.0014
HV7a	59.5652	0.1199	0.2928	0.0033	0.4375	0.0117	0	0.0055	0.0051	0.0011	0.001	0.0002	0	0.0005	0.0005
HV7b	60.6725	0.1232	0.1949	0.0028	0.3116	0.0108	0	0.0059	0.0043	0.0011	0.001	0.0003	0	0.0005	0.0005
HV7c	59.551	0.119	0.2686	0.0031	0.446	0.0117	0	0.0056	0.0036	0.001	0.0009	0.0002	0.0003	0.0001	0.0004
HV7d	58.67	0.1208	0.362	0.0037	0.4607	0.0119	0	0.0057	0.0058	0.0011	0.0008	0.0002	0	0.0005	0.0008
HV7e	59.0718	0.1193	0.3719	0.0037	0.6353	0.0133	0.0055	0.0015	0.0037	0.001	0.001	0.0002	0	0.0005	0.0006
HV7f	59.2924	0.1193	0.2972	0.0033	0.4266	0.0115	0	0.0056	0.0037	0.001	0.0013	0.0003	0	0.0005	0.0003
A12a	59.4706	0.1214	0.121	0.0021	1.3922	0.019	0	0.0057	0	0.0852	0.0046	0.0003	0.0005	0.0001	0.0008
A12b	58.7967	0.1199	0.0911	0.0019	1.0521	0.0166	0	0.0057	0	0.0841	0.0024	0.0003	0	0.0005	0.0007
A12c	59.1531	0.1205	0.0879	0.0018	1.1041	0.0171	0	0.0056	0	0.0841	0.0024	0.0003	0.0004	0.0001	0.0007
A12d	58.9705	0.1204	0.104	0.002	1.0065	0.0164	0	0.0056	0	0.0843	0.002	0.0003	0.0004	0.0001	0.0007
A12e	59.2914	0.1202	0.1023	0.002	1.2368	0.0178	0.0051	0.0015	0	0.0835	0.002	0.0003	0	0.0005	0.0007
A12f	58.4885	0.121	0.0773	0.0017	1.0462	0.0167	0	0.0057	0	0.0824	0.002	0.0003	0.0003	0.0001	0.0008

Table 1. pXRF measurements from Spring 2022. Faces of cubes labeled a-f.

Site	Source	Specimen	Name	Mass (kg)	Volume Susceptibility (Hi)	Volume Susceptibility (Lo)	Mass Susceptibility (Hi)	Mass Susceptibility (Lo)	A	B	C	D	E	F
Sedgefield	DM	2	DM-2	0.0169217	0.00000	-0.00001	0.00000	-0.00059	-1	-1	-1	-2	-1	-2
Sedgefield	DM	15	DM-15	0.0176723	0.00001	-0.00001	0.00057	-0.00057	-2	-3	-2	-3	-2	-2
Sedgefield	DM	22	DM-22	0.0164874	0.00000	-0.00001	0.00000	-0.00061	-2	-2	-2	-2	-2	-1
Sedgefield	DM	23	DM-23	0.0192154	0.00000	-0.00001	0.00000	-0.00052	-1	0	-1	0	-1	0
Sedgefield	DM	29	DM-29	0.0191892	-0.00001	-0.00001	-0.00052	-0.00052	-1	0	0	0	0	-1
Sedgefield	DM	30	DM-30	0.0150583	0.00000	-0.00001	0.00000	-0.00066	0	-1	-1	0	0	0
Sedgefield	DM		Average	0.0174241	0.00000	-0.00001	0.00000	-0.00057						
Albertinia	A	12	A-12	0.0165163	0.00000	-0.00001	0.00000	-0.00061	0	0	0	0	0	-1
Albertinia	A	15	A-15	0.0213234	-0.00001	-0.00001	-0.00047	-0.00047	-1	-2	-1	-1	-1	-1
Albertinia	A	18	A-18	0.0213264	0.00000	-0.00002	0.00000	-0.00094	-1	-1	-1	-1	-1	-1
Albertinia	A	27	A-27	0.0183256	-0.00001	0.00000	-0.00055	0.00000	-1	-1	0	-1	-1	-1
Albertinia	A	49	A-49	0.0190428	-0.00001	0.00000	-0.00053	0.00000	-1	-1	-1	-1	-1	-1
Albertinia	A	60	A-60	0.0186784	-0.00001	-0.00001	-0.00054	-0.00054	-1	0	-1	-1	0	0
Albertinia	A		Average	0.0192022	-0.00001	-0.00001	-0.00035	-0.00043						
Hunter Valley	HV	7	HV-7	0.0207333	0.00001	0.00002	0.00048	0.00096	2	1	2	2	1	2
Hunter Valley	HV	13	HV-13	0.0166957	0.00000	0.00001	0.00000	0.00060	3	3	3	2	3	3
Hunter Valley	HV	33	HV-33	0.0177577	0.00000	0.00002	0.00000	0.00113	3	3	2	2	3	3
Hunter Valley	HV	40	HV-40	0.0172611	0.00000	0.00002	0.00000	0.00116	2	3	2	2	1	2
Hunter Valley	HV	41	HV-41	0.0183667	0.00001	0.00001	0.00054	0.00054	2	1	2	2	2	2
Hunter Valley	HV	48	HV-48	0.0179681	0.00000	0.00001	0.00000	0.00056	2	2	1	2	3	1
Hunter Valley	HV		Average	0.0181304	0.00000	0.00002	0.00018	0.00083						
George	G	2	G-2	0.0174527	-0.00002	-0.00001	-0.00115	-0.00057	-1	-2	-2	-1	-2	-2
George	G	15	G-15	0.0167932	-0.00002	-0.00001	-0.00119	-0.00060	-1	-2	-1	-2	-2	-1
George	G	20	G-20	0.0186610	-0.00002	-0.00001	-0.00107	-0.00054	-1	-1	-1	-1	-2	-1
George	G	24	G-24	0.0185452	-0.00002	-0.00001	-0.00108	-0.00054	-2	-1	-2	-1	-2	-2
George	G	25	G-25	0.0176293	-0.00002	-0.00002	-0.00113	-0.00113	-1	1	-2	-1	-2	-1
George	G	36	G-36	0.0217289	-0.00002	-0.00002	-0.00092	-0.00092	-2	-2	-2	-2	-1	-2
George	G		Average	0.0184684	-0.00002	-0.00001	-0.00108	-0.00072						
Clanwilliam	AF	3	AF-3	0.0236261	0.00017	0.00017	0.00720	0.00720	14	18	18	16	10	15
Clanwilliam	AF	5	AF-5	0.0204063	0.00014	0.00014	0.00686	0.00686	16	15	20	18	15	18
Clanwilliam	AF	11	AF-11	0.0205153	0.00011	0.00011	0.00536	0.00536	13	13	13	12	12	15
Clanwilliam	AF	26	AF-12	0.0210541	0.00010	0.00009	0.00475	0.00427	13	11	10	12	8	13
Clanwilliam	AF	28	AF-13	0.0190111	0.00006	0.00005	0.00316	0.00263	7	7	9	8	8	7
Clanwilliam	AF	32	AF-14	0.0197502	0.00012	0.00011	0.00608	0.00557	12	13	15	16	17	12
Clanwilliam	AF		Average	0.0207272	0.00012	0.00011	0.00563	0.00539						

Table 2. Magnetic susceptibility measurements from Spring 2022.

Sample	Step	Weight (g)	Hi Susceptibility (m³/kg)	Low Susceptibility (m³/kg)	L	A	B
A15	NRM	10.8556	7.40E-09	7.00E-09	83.27	-1.114	17.625
A15	100	10.8407	6.00E-10	4.30E-09	85.95	1.058	16.801
A18	NRM	9.0032	7.90E-09	-7.40E-09	84.77	-1.487	18.915
A18	100	8.9945	3.30E-09	2.90E-09	78.55	-0.876	14.29
A49	NRM	8.7075	8.67E+00	0	75.09	-3.346	14.719
A49	100	8.697	1.10E-09	0	80.16	-0.806	19.246
A60	NRM	7.5198	8.20E-09	-4.30E-09	77.19	-3.265	13.584
A60	100	7.4877	1.50E-09	2.60E-09	82.5	-0.094	15.643
AF3	NRM	10.0913	6.26E-08	6.24E-08	72.05	7.844	7.875
AF3	100	10.0319	6.25E-08	6.20E-08	50.34	12.711	10.561
AF26	NRM	21.0238	5.16E-08	5.27E-08	54.51	11.531	12.254
AF26	100	21.0131	5.07E-08	5.36E-08	58.41	19.537	16.363
AF28	NRM	18.6427	3.66E-08	4.10E-08	56.71	11.989	11.669
AF28	100	18.6345	3.75E-08	4.10E-08	55.61	14.7	13.789
AF32	NRM	9.6046	5.92E-08	6.26E-08	67.73	9.587	23.981
AF32	100	9.5434	6.65E-08	5.96E-08	63.4	13.223	27.134
DM22	NRM	16.3493	0	2.50E-09	79.47	6.193	26.807
DM22	100	16.3485	-1.70E-09	-2.00E-09	81	6.557	26.556
DM23	NRM	18.8243	1.60E-09	3.99E-10	77.43	27.078	25.724
DM23	100	18.8217	1.10E-09	8.00E-10	74.96	29.058	30.9
DM29	NRM	19.0707	-	-	82.9	3.571	27.901
DM29	100	19.0662	-7.00E-12	2.00E-10	81.69	5.355	31.16
DM30	NRM	14.9991	-	-	73.76	7.713	24.787
DM30	100	14.9963	3.60E-09	-8.00E-10	72.15	9.597	29.29
G20	NRM	18.2478	-	-	73.62	-2.846	15.103
G20	100	18.2462	4.00E-10	4.50E-09	77.06	-1.166	16.49
G24	NRM	18.5009	-	-	70.36	-4.15	11.336
G24	100	18.4989	-1.90E-09	-2.70E-09	73.65	-1.89	14.797
G25	NRM	9.3283	-3.40E-09	-5.40E-09	75.78	-1.584	15.166
G25	100	9.3063	-2.40E-09	-1.20E-09	72.63	1.907	18.975
G36	NRM	9.0867	-1.54E-08	-4.20E-09	80.83	-3.345	18.961
G36	100	9.085	-2.20E-09	-4.10E-09	82.36	-1.163	22.797
HV7	NRM	19.8882	-	-	68.65	4.344	24.968
HV7	100	19.8793	1.10E-08	1.16E-08	68.54	9.015	25.14
HV40	NRM	17.0017	-	-	63.68	5.133	27.489
HV40	100	17.0013	1.36E-08	1.18E-08	64.14	10.273	27.772
HV41	NRM	18.2304	-	-	74.92	0.869	21.572
HV41	100	18.2298	1.20E-08	1.41E-08	78.66	3.914	29.631
HV48	NRM	17.6689	-	-	83.13	-1.88	19.471
HV48	100	17.6685	2.10E-09	-1.46E-08	83.09	4.385	19.144

Table 3. Table of measurements from experiments begun Fall 2022. Color reported in LAB color space (L: lightness; A: red/green value; B: blue/yellow value).

References

Brain, C.K., Sillen, A., 1988. Evidence from the Swartkrans cave for the earliest use of fire Nature, 336, pp. 464-466

Brown K. S., Marean C. W., Herries A. I. R., Jacobs Z., Tribolo C., Braun D., Roberts D. L., Meyer M. C., & Bernatchez J., 2009. Fire As an Engineering Tool of Early Modern Humans. Science, 325(5942), pp. 859–862.

Brown, M.C., Hervé, G., Korte, M. and Genevey, A., 2021. Global archaeomagnetic data: The state of the art and future challenges. Physics of the Earth and Planetary Interiors, 318, pp. 106766.

Butler, R.F., 1992. *Paleomagnetism: magnetic domains to geologic terranes* (Vol. 319). Boston: Blackwell Scientific Publications.

Calvo-Rathert, M., Carrancho, Á., Stark, F., Villalaín, J. J., & Hill, M., 2012. Are burnt Sediments reliable recorders of geomagnetic field strength? Quaternary Research, 77(2), 326–330.

Carrancho, A., Villalaín, J., Vallverdú Poch, J., & Carbonell, E., 2016. Is it possible to identify temporal differences among combustion features in Middle Palaeolithic palimpsests? The archaeomagnetic evidence: A case study from level O at the Abric Romaní rock-shelter (Capellades, Spain). Quaternary International, 417, pp. 39-50.

Collinson, J.D., 1978. Deserts H.G. Reading (Ed.). Sedimentary Environments and Facies. Blackwell, Oxford, pp. 15-60

Dunlop, D.J., 1972. Magnetic mineralogy of unheated and heated red sediments by coercivity spectrum analysis. Geophysical Journal International, 27(1), pp. 37-55.

Eighmy, J. L., & Sternberg, R. S., 1990. Archaeomagnetic Dating. University of Arizona Press.

Frahm, E. and Feinberg, J.M., 2013a. Environment and collapse: Eastern Anatolian obsidians at Urkesh (Tell Mozan, Syria) and the third-millennium Mesopotamian urban crisis. Journal of Archaeological Science, 40(4), pp.1866-1878.

Frahm, E., & Feinberg, J. M., 2013b. From flow to quarry: Magnetic properties of obsidian and changing the scale of archaeological sourcing. Journal of Archaeological Science, 40(10), 3706–3721.

Frahm, E., & Hauck, T. C., 2017. Origin of an obsidian scraper at Yabroud Rockshelter II (Syria): Implications for Near Eastern social networks in the early Upper Palaeolithic. Journal of Archaeological Science: Reports, 13, pp. 415–427.

Harrison R., 2004. Kimberley points and colonial preference: new insights into the chronology of pressure flaked point forms from the southeast Kimberley, Western Australia. Archaeol. Oceania 39(1), pp. 1-11.

James, S. R., Dennell, R. W., Gilbert, A. S., Lewis, H. T., Gowlett, J. A. J., Lynch, T. F., McGrew, W. C., Peters, C. R., Pope, G. G., Stahl, A. B., & James, S. R., 1989. Hominid Use of Fire in the Lower and Middle Pleistocene: A Review of the Evidence [and Comments and Replies]. Current Anthropology, 30(1), pp. 1–26.

Lin, S.-N., Huang, C.-C., Wu, M.-T., Wang, W.-L. and Hsieh, K.-C., 2017. Crucial Mechanism to the Eutectoid Transformation of Wüstite Scale on Low Carbon Steel. Steel Research Int., 88(11), pp.1700045.

Mackay, A., Lin, S.C., Kenna, L.S. and Blackwood, A.F., 2019. Variance in the response of silcrete to rapid heating complicates assumptions about past heat treatment methods. Archaeological and Anthropological Sciences, 11(11), pp.5909-5920.

Mazz, J.M.L., 2017. Silcrete procurement system in Uruguayan prehistory. Journal of Archaeological Science: Reports, 15, pp.561-569.

Mourre, V., Villa, P. and Henshilwood, C.S. 2010. Early use of pressure flaking on lithic artifacts at Blombos Cave, South Africa. Science, 330(6004), pp.659-662.

Nami, H.G., 2017. Silcrete as a valuable resource for stone tool manufacture and its use by Paleo-American hunter–gatherers in southeastern South America. Journal of Archaeological Science: Reports, 15, pp.539-560.

Nash, D.J., Thomas, D.S. and Shaw, P.A., 1994. Siliceous duricrusts as palaeoclimatic indicators: evidence from the Kalahari Desert of Botswana. Palaeogeography, Palaeoclimatology, Palaeoecology, 112(3-4), pp.279-295.

Nash D. J. & Shaw, P. A., 1998. Silica and carbonate relationships in silcrete-calcrete intergrade duricrusts from the Kalahari of Botswana and Namibia. Journal of African Earth Sciences 27, pp.11–25

Nash, D.J., Coulson, S., Staurset, S., Ullyott, J.S., Babutsi, M., Hopkinson, L. and Smith, M.P., 2013a. Provenancing of silcrete raw materials indicates long-distance transport to Tsodilo Hills, Botswana, during the Middle Stone Age. Journal of Human Evolution, 64(4), pp. 280-288.

Nash, D.J., Coulson, S., Staurset, S., Smith, M.P. and Ullyott, J.S., 2013b. Provenancing silcrete in the Cape coastal zone: implications for Middle Stone Age research in South Africa. Journal of Human Evolution, 65(5), pp. 682-688.

Pickering, T.R., Egeland, C.P., Domínguez-Rodrigo, M., Brain, C.K. and Schnell, A.G., 2008. Testing the "shift in the balance of power" hypothesis at Swartkrans, South Africa: hominid cave use and subsistence behavior in the Early Pleistocene. Journal of Anthropological Archaeology, 27(1), pp. 30-45.

Rowney, M. & White, P. J., 1997. Detecting Heat Treatment on Silcrete: Experiments with Methods. Journal of Archaeological Science, 24(7), pp. 649-657.

Salomon, H., Vignaud, C., Coquinot, Y., Beck, L., Stringer, C., Strivay, D., & D'errico, F., 2012. Selection and Heating of Colouring Materials in the Mousterian Level of Es-Skhul (C. 100 000 Years Bp, Mount Carmel, Israel). Archaeometry, 54(4), pp. 698–722.

Schmidt, P., Masse, S., Laurent, G., Slodczyk, A., Le Bourhis, E., Perrenoud, C., Livage, J. and Fröhlich, F., 2012. Crystallographic and structural transformations of sedimentary chalcedony in flint upon heat treatment. Journal of Archaeological Science, 39(1), pp.135-144.

Schmidt, P., Porraz, G., Slodczyk, A., Bellot-Gurlet, L., Archer, W. and Miller, C.E., 2013. Heat treatment in the South African Middle Stone Age: temperature induced transformations of silcrete and their technological implications. Journal of Archaeological Science, 40(9), pp. 3519-3531.

Schmidt, P., Lauer, C., Buck, G., Miller, C.E. and Nickel, K.G., 2017. Detailed near-infrared study of the 'water'-related transformations in silcrete upon heat treatment. Physics and Chemistry of Minerals, 44(1), pp. 21-31.

Summerfield, M.A., 1982. Distribution, nature and genesis of silcrete in arid and semi-arid southern Africa. Catena, Supplement, 1, pp. 37-65

Summerfield MA., 1983a. Silcrete. In Chemical Sediments and Geomorphology, Goudie AS, Pye K (eds). Academic Press: London, pp. 59–91.

Summerfield MA., 1983b. Petrography and diagenesis of silcrete from the Kalahari Basin and Cape Coastal Zone, southern Africa. Journal of Sedimentary Petrology 53, pp. 895–909.

Summerfield, M.A., 1983c. Silcrete as a palaeoclimatic indicator: evidence from southern Africa. Palaeogeography, Palaeoclimatology, Palaeoecology, 41(1-2), pp. 65-79.

Tauxe, L., Mullender, T.A.T. and Pick, T., 1996. Potbellies, wasp-waists, and superparamagnetism in magnetic hysteresis. Journal of Geophysical Research: Solid Earth, 101(B1), pp. 571-583.

Thiry, M. & Milnes, A., 1991. Pedogenic and groundwater silcretes at Stuart Creek opal field, South Australia. Journal of Sedimentary Research, 61(1), pp. 111–127.

Thiry, M. and Ribet, I., 1999. Groundwater silicification in Paris Basin limestones; fabrics, mechanisms, and modeling. Journal of Sedimentary Research, 69(1), pp.171-183.

Ullyott, J.S. and Nash, D.J., 2016. Distinguishing pedogenic and non-pedogenic silcretes in the landscape and geological record. Proceedings of the Geologists' Association, 127(3), pp. 311-319.

Watson, S., Nasoordeen, S., Grote, M.N., Mackay, A. and Schmidt, P., 2021. What causes differences in fracture rates of silcrete during heat treatment? A near-infrared study of water-related transformations in South African silcretes. Journal of Archaeological Science: Reports, 39, pp. 103162.

Webb, J.A. and Domanski, M., 2008. The relationship between lithology, flaking properties and artefact manufacture for Australian silcretes. Archaeometry, 50(4), pp. 555-575.